Laser Induced Aluminum Surface Breakdown Model

Final Report

Contract Number: H-33325D

Prepared for

National Aeronautics and Space Administration
George C. Marshall Space Flight Center
Marshall Space Flight Center, AL 35812

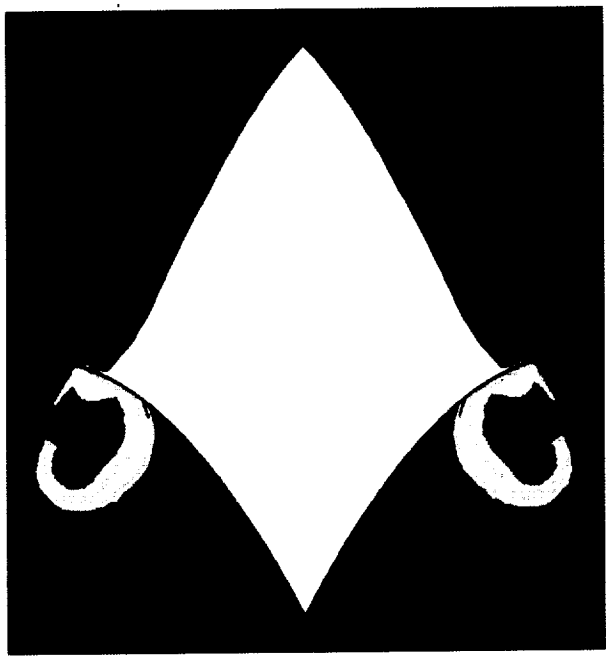

by

Y. S. Chen, J. Liu and S. Zhang

Engineering Sciences, Inc.
1900 Golf Road, Suite D
Huntsville, AL 35802
(256) 883-6233

June 25, 2002

Laser Induced Aluminum Surface Breakdown Model

PROJECT SUMMARY

Laser powered propulsion systems involve complex fluid dynamics, thermodynamics and radiative transfer processes. Based on an unstructured grid, pressure-based computational aerothermodynamics platform, several sub-models describing such underlying physics as laser ray tracing and focusing, thermal non-equilibrium, plasma radiation and air spark ignition have been developed. This proposed work shall extend the numerical platform and existing sub-models to include the aluminum wall surface Inverse Bremsstrahlung (IB) effect from which surface ablation and free-electron generation can be initiated without relying on the air spark ignition sub-model. The following tasks will be performed to accomplish the research objectives.

An aluminum surface ablation-ionization model is developed to provide surface temperature rise and the generation of seed electron concentration in the laser focal region that is required for initiate the air breakdown process. A simplified heat conduction equation is employed to calculate the temperature evolution of the aluminum surface, which is in tern used for the calculation of aluminum ionization near the surface.

The coupling of the aluminum surface breakdown model with the computational fluid dynamics model developed for pulse laser supported propulsion system allows the simulation to start without the assumption of using a spark ignition heat source. Benchmark testing of the present model for laser Lightcraft model-200 has shown the effectiveness of the present model. The only remaining tunable modeling constant of the present model is in calculating the effective laser absorption coefficient based on the level of ionization of air plasma.

INTRODUCTION

Currently, NASA's aim of operating low cost launch and space vehicles requires the research and development of advanced propulsion technologies and concepts. One plausible advanced concept is the utilization of off-board pulsed laser power source to propel small payload (e.g. 100kg) into earth orbit. The merit of the laser-propelled vehicles is in its high efficiency (do not need to carry fuel) and high specific impulse. Previous SDIO research led to the invention of the one of the laser powered launch vehicle concept – the Laser Lightcraft concept, currently being tested at the High Energy Laser Test System Facility, White Sands Missile Range, New Mexico. Although the spin-stabilized small scale Lightcraft model (invented by Myrabo) has been flown successfully up to an altitude of 30 meters using a 10 kW pulsed-laser at 10 Hz, many technical issues need to be addressed before an optimized design of the vehicle and its operation can be achieved.

The purpose of this study is to establish the technical ground for modeling the physics of laser powered pulse detonation phenomenon. The principle of the laser power propulsion is that when high-powered laser is focused at a small area near the surface of a thruster, the intense energy causes the electrical breakdown of the working fluid (e.g. air) and forming high speed plasma (known as the inverse Bremsstrahlung, IB, effect). The intense heat and high pressure created in the plasma consequently causes the surrounding to heat up and expand until the thrust producing shock waves are formed. This complex process of gas ionization, increase in radiation absorption and the forming of plasma and shock waves will be investigated in the development of the present numerical model. In the first phase of this study, laser light focusing, radiative absorption and shock wave propagation over the entire pulsed cycle are modeled. The model geometry and test conditions of known benchmark experiments such as those in Myrabo's experiment will be employed in the numerical model validation simulations. The calculated performance data (e.g. coupling coefficients) will be compared to the test data. Plans for the numerical

modeling of the detailed IB effect will also be described in the proposed investigation. The final goal will be the design analysis of the full-scale laser propelled flight vehicle using the present numerical model.

In previous study, Engineering Sciences, Inc. has developed a laser powered launch vehicle performance analysis tool based on its in-house flow and radiation codes. UNIC-UNS unstructured-grid flow code and GRADP-UNS unstructured-grid radiation code are two advanced numerical models. Many complex engineering design problems related to fluid dynamics and radiative heat transfer have been solved using these two codes. High-temperature thermodynamics and plasma dynamics models have been developed with benchmark data validations presented for laser powered launch vehicles. The development work has included transient shock capturing algorithm using unstructured-grid method with dynamic local refinement and coarsening adaptive grid strategy. High temperature thermodynamics and plasma gas dynamics physics are modeled and validated. Non-equilibrium radiation model with the effects of gas breakdown and laser energy absorption has also been addressed and modeled. These advanced thermodynamics and radiation models serve as the fundamental building blocks for the present model development and for the ultimate utilization of the laser powered launch vehicle performance analysis tool in real designs.

In the present research, the development work for modeling the mechanisms for initializing the aluminum surface ablation and ionization due to focused laser energy is completed and tested for a laser Lightcraft model-200. At the start of the laser pulse, the beams are focused at a small area on the aluminum surface of the test vehicle. Part of the energy is absorbed by the material and causes to overcome the bounding energy of the molecules. According to Harada [1-4], this process is accounted for through stopping power that is caused by collisions between ions and atoms of the material. Since the energy source is different in the present application that laser beam instead of ion beam is the energy source, the energy source modeling would consider the absorption of radiative energy at the wall surface. In the present case, the energy

absorbed, as output from the radiation model, is used to calculate the heat conduction and energy balance at the wall surface through which the ablation rates of the aluminum material from the surface is calculated. The ionization of the ablated material is then initiated by using the Saha-Eggert equation under the thermal and chemical equilibrium assumption [4]. The developed model is described below.

COMPUTATIONAL FLUID DYNAMICS MODEL

Governing Equations

For The Continuity, Navier-Stokes and Energy (Total Enthalpy) Equations, can be written in a Cartesian tensor form:

$$\frac{\partial \rho}{\partial t}+\frac{\partial}{\partial x_j}\left(\rho u_j\right)=0 \tag{1}$$

$$\frac{\partial \rho u_i}{\partial t}+\frac{\partial}{\partial x_j}\left(\rho u_j u_i\right)=-\frac{\partial p}{\partial x_i}+\frac{\partial \tau_{ij}}{\partial x_j} \tag{2}$$

$$\frac{\partial \rho H}{\partial t}+\frac{\partial}{\partial x_j}\left(\rho u_j H\right)=\frac{\partial p}{\partial t}+Q_{ec}+Q_v+\frac{\partial}{\partial x_j}\left(\frac{\mu}{P_r}\nabla H\right)+\frac{\partial}{\partial x_j}\left(\left(1-\frac{\mu}{P_r}\right)\nabla\left(V^2/2\right)\right) \tag{3}$$

$$\frac{\partial}{\partial t}\left(\frac{2}{3}k_b n_e T_e\right)+\frac{\partial}{\partial x_j}\left(\frac{2}{3}k_b n_e T_e u_j\right)=\frac{\partial}{\partial x_j}\left(\lambda_e \frac{\partial T_e}{\partial x_j}\right)+Q_r-Q_{ec} \tag{4}$$

where ρ is the fluid density, u_i is the i^{th} Cartesian component of the velocity, p is the static pressure, μ is the fluid viscosity, P_r is the Prandtl number, H is the gas total enthalpy and V stands for the sum of velocity squared. In Eq. (4), k_b, n_e, T_e, λ_e, Q_r, Q_v and Q_{ec} are the Boltzmann's constant, electron number density, electron temperature, electron thermal conductivity, radiative heat source from laser absorption and radiative transfer, vibrational-translation energy transfer source term, and the energy transfer due to eletron/particle elastic collisions, respectively. The shear stress τ_{ij} can be expressed as:

$$\tau_{ij} = (\mu + \mu_t)\left(\frac{\partial u_i}{\partial x_j} + \frac{\partial u_j}{\partial x_i} - \frac{2}{3}\frac{\partial u_k}{\partial x_k}\delta_{ij}\right) - \frac{2}{3}\rho k \delta_{ij}$$

The species conservation equation is expressed as:

$$\frac{\partial \rho Y_i}{\partial t} + \frac{\partial}{\partial x_j}\left(\rho u_j Y_i\right) = \frac{\partial}{\partial x_j}\left[\left(\rho D + \frac{\mu_t}{\sigma_Y}\right)\frac{\partial Y_i}{\partial x_j}\right] + \dot{\omega}_i$$

where Y_i is the i^{th} species mass fraction, D is the mass diffusivity, σ_Y is the turbulent Schmidt number, and $\dot{\omega}_i$ is the chemical reaction rate for species i respectively.

Vibrational Energy Equation

For high temperature gas flows, thermal non-equilibrium state may be important. In Landau and Teller's derivation, a master equation is employed to describe the evolution of the population of quantum level N_i. This master equation is written as:

$$\frac{dN_i}{dt} = N\sum_{j=0}^{I_{\max}} K_{j\Rightarrow i} N_j - N\sum_{j=0}^{I_{\max}} K_{i\Rightarrow j} N_i; \quad i = 0,1,2,\ldots,I_{\max}$$

Results from the quantum mechanical solution of the harmonic oscillator are used to relate the various quantum transition rates to one another, and then the master equation may be summed over all quantum states to arrive at the Landau-Teller equation:

$$\frac{D\rho e_v}{Dt} = \frac{\partial}{\partial x_i}\left(k_v \frac{\partial T_v}{\partial x_i}\right) + \rho\frac{e_v^{eq}(T_t) - e_v}{\tau_{LT}} \approx \frac{\partial}{\partial x_i}\left(k_v \frac{\partial T_v}{\partial x_i}\right) + \rho\frac{C_{v,v}(T - T_v)}{\tau_{LT}}$$

where ρ, e_v, e_v^{eq} and τ_{LT} represent the gas density, vibrational energy, effective (equilibrium) vibrational energy and the vibrational-translational relaxation time scale respectively. An empirical expression (to be discussed in the next section) is used to model the Landau-Teller relaxation time scale.

As discussed by Gnoffo (1989), the vibrational-translation energy relaxation time scale can be evaluated using the following equation

$$\tau_{LT} = \frac{\sum_{s=mol.} \rho_s / M_s}{\sum_{s=mol.} \rho_s / M_s < \tau_s >}$$

and

$$< \tau_s >= \tau_s^{MW} + \tau_s^P$$

$$\tau_s^P = \left(\sigma_s \bar{c}_s n_s \right)^{-1}$$

$$\bar{c}_s = \left(8 k_b T / \pi m_s \right)^{1/2}$$

$$\tau_s^{MW} = \frac{\sum_{j=1}^{10} n_j \exp\left[A_s \left(T^{-1/3} - 0.015 \mu_{sj}^{1/4} \right) - 18.42 \right]}{p \sum_{j=1}^{10} n_j}$$

where subscript s represents the participating species (only diatomic species are involved here). σ, n, m and μ denote the effective cross section, species number density, species unit mass and reduced molecular weight, respectively. The correlation constant, A_s, has different values for each participating species. They are given in the table below.

Table 1. Correlation constants for modeling the vibrational relaxation time.

s	Ms	As
N2	28	220
O2	32	129
N	14	0
O	16	0
NO	30	168
N+	14	0
O+	16	0
N2+	28	220
O2+	32	129
NO+	30	168
e-	.0005486	0

Three-Temperature Energy Equations Point Implicit Coupling

For solution accuracy and stability, a point-implicit procedure is employed for solving the coupled three-temperature energy equations. The three-temperature energy equations in time domain can be written as:

$$\rho\frac{\partial h_g}{\partial t} = -C_{coll}\left(T_g - T_e\right) - \sum_i \frac{\rho_s}{\tau_s}\left(e^*_{v,s} - e_{v,s}\right)$$

$$\rho\frac{\partial e_v}{\partial t} = \sum_i \frac{\rho_s}{\tau_s}\left(e^*_{v,s} - e_{v,s}\right)$$

$$\rho\frac{\partial e_e}{\partial t} = C_{coll}\left(T_g - T_e\right) + Q_r$$

where C_{coll} represents the elastic-inelastic collision energy transfer coefficient. The left-hand-side terms of the above equations can be discretized as:

$$\rho\frac{\partial h}{\partial t} = \rho\left(\frac{\partial h}{\partial T}\right)\frac{\partial T}{\partial t} = \rho C_p \frac{\partial T}{\partial t} \approx \rho C_p \frac{\left(T^{n+1} - T^n\right)}{\Delta t}$$

$$\rho\frac{\partial e}{\partial t} = \rho\left(\frac{\partial e}{\partial T}\right)\frac{\partial T}{\partial t} = \rho C_v \frac{\partial T}{\partial t} \approx \rho C_v \frac{\left(T^{n+1} - T^n\right)}{\Delta t}$$

The last term in the above equations represent finite difference discretization. Also, applying the simplifying assumption for the vibrational energy relaxation term: (see Peter A. Gnoffo's NASA TP-2867, page 17, Eqs. 59 – 61)

$$\sum_i \frac{\rho_s}{\tau_s}\left(e^*_{v,s} - e_{v,s}\right) \approx \rho\frac{C_{v,v}}{\bar{\tau}}\left(T_g - T_v\right)$$

The final linearized equations are written in matrix form:

$$\begin{bmatrix} \left(\rho\frac{C_{p,g}}{\Delta t}+C_{coll}+\rho\frac{C_{v,v}}{\bar{\tau}}\right) & -\rho\frac{C_{v,v}}{\bar{\tau}} & -C_{coll} \\ -\rho\frac{C_{v,v}}{\bar{\tau}} & \left(\rho\frac{C_{v,v}}{\Delta t}+\rho\frac{C_{v,v}}{\bar{\tau}}\right) & 0 \\ -C_{coll} & 0 & \left(\rho\frac{C_{v,e}}{\Delta t}+C_{coll}\right) \end{bmatrix} \begin{Bmatrix} T_g^{n+1} \\ T_v^{n+1} \\ T_e^{n+1} \end{Bmatrix} =$$

$$\begin{bmatrix} \rho\frac{C_{p,g}}{\Delta t} & 0 & 0 \\ 0 & \rho\frac{C_{v,v}}{\Delta t} & 0 \\ 0 & 0 & \rho\frac{C_{v,e}}{\Delta t} \end{bmatrix} \begin{Bmatrix} T_g^{n} \\ T_v^{n} \\ T_e^{n} \end{Bmatrix} + \begin{Bmatrix} 0 \\ 0 \\ Q_r \end{Bmatrix}$$

Aluminum Wall Energy Equation

The energy balance of the aluminum wall material is described by a 1-D heat conduction equation with energy input at one end with material ablation rates. That is,

$$\rho_w \frac{dH_w}{dt} = \frac{d}{dx}\left(k\frac{dT_w}{dx}\right) + A\left(Q_r - \dot{m}\Delta H\right), \qquad A = 1 \; at \; surface, 0 \; otherwise$$

where the subscript $_w$ stands for wall material, Q_r is the energy input due to absorption of radiative energy, $\dot{m}$ denotes the ablation rates and ΔH is the ablation energy that includes the latent heat of evaporation. In the present model, the surface energy absorption of the laser energy is calculated through the ray-tracing module. All near wall cells that are active due to energy absorption is then analyzed for the thermal conditions based on the above heat conduction equation. The density of the ablated aluminum atoms in the near wall cell is than calculated based on the following equation.

$$\frac{D\rho_{AL}}{Dt} = \dot{m}$$

Wall cells (elements) subjected to laser absorption are registered and counted after the laser ray tracing process. The 1-D heat conduction models for these

wall points are solved for the wall surface temperature evolution. The outside wall is assumed to be always isothermal at 300 K. For simplicity, the aluminum atom generation is ignored in the present model. It is found that only the calculation of electron concentration production rate is important for initiating the air breakdown process.

Ionization Modeling

The resultant surface temperature and ablation rates are then used for material ionization calculation through the Saha-Eggert equation. That is,

$$S_r(T) = \frac{n_{r+1} n_e}{n_r} = \frac{2U_{r+1}(T)}{U_r(T)} \frac{(2\pi m_e kT)^{3/2}}{h^3} e^{-\frac{E_r - \Delta E_r}{kT}}$$

where n stands for number density (1/cm^3), r denotes the r-fold ionization level, e denotes electronic property, U is the partition function of ionization potential, me is the rest mass of electron (= 9.108E-28 g), k is the Boltzmann's constant (=1.381E-16 erg/deg-K) and h is the Plank's constant (= 6.626E-27 erg-sec). For first-fold ionization (r=0, $AL \rightarrow AL^+ + e^-$ and $n_{AL+} = n_e$), the above equation can be written as (after plugging in all constants):

$$\frac{n_e^2}{n_{AL+}} = 2.415130256 \times 10^{15} \frac{2U_1}{U_0} T^{3/2} e^{-\frac{E_0 - \Delta E_0}{kT}}$$

where the Unsold's formula for the lowering of ionization energy is used here. That is, $\Delta E_0 = 6.96 \times 10^{-7} (n_e)^{1/3} Z_{eff}^{2/3}$ $(in\ eV)$, $and\ Z_{eff} = \frac{\sum_{i=1}^{r+2} Z_i^2 n_i}{n_e} = 1\ for\ r = 0$. Also, E_0 = 5.984 eV for aluminum (1 eV = 1.602x10^{-12} erg). Tabulate values for U1 from [5] is generated for the present model.

A module for the aluminum surface ablation has been developed and tested. To apply the present model to the laser lighcraft aluminum-surface-breakdown process, the aluminum surface emissivity is needed to start the

calculation. Some emissivity data for aluminum is given in the following table [6]. For the present application, aluminum emissivity of 0.1 is used in the simulation. This means that 90% of the laser energy is absorbed at the focal region, which gives very rapid temperature rise and creates high values of aluminum ablation rates for subsequent ionization. High values of electron number density are generated as a result of the ionization process.

Table 2. Aluminum surface emissivity property.

Aluminum Material	Temp., °F	Emissivity
Highly Polished Plate, 98.3% pure	440 – 1070	0.039 – 0.057
Commercial Sheet	212	0.09
Heavily Oxidized	299 – 940	0.20 – 0.31
AL-Surfaced Roofing	100	0.216

Code Modification for Efficiency

The UNIC-UNS pulsed laser supported propulsion numerical model is further modified to enable parallel computing for efficient computations, especially for three-dimensional models. The ray tracing radiative heat transfer model, laser ray inlet boundary conditions, laser reflection conditions, thrust force time integration and performance data integration are implemented to work in parallel computing environment. Full 3D ray tracing radiation model is also implemented in this task. This model has been tested successfully using 2D and 3D laser lightcraft model-A configuration and test conditions.

A new treatment for modeling the laser absorption when the local electron number density reaches the resonant critical value has been developed to remove the difficulty of calculating short pulse width conditions due to very high laser power. Previously, a resonant absorption constant is assumed as soon as the local electron number density reaches the critical value. This creates a step jump in energy input to the local computational cells and causes the instability of the numerical model. To circumvent this problem, a smooth variation in the

energy absorption is assumed before the laser rays reach the plasma resonance front. This smooth absorption function is constructed based on the electron number density. Preliminary calculation using this treatment showed increased integrated thrust coupling coefficients for normal pulse width cases. Test for a short pulse-width case (with 1 microsecond pulse width) has shown good stability of the computational model. Fine-tuning of this treatment is necessary to anchor the modeling constants for its applicability over a selected range of pulse widths and power levels. Further research is required to test the present model for Lightcraft performance calculations with short pulse width conditions.

MODEL-200 PERFORMANCE ALANYSIS

The present model is tested for the laser Lightcraft Model-200-3/4 and compared with experimentally measured data for a range of laser power levels. Two models are used for comparison purpose. The spark ignition model is used to provide the baseline of the predictions. Then, the same cases are computed with the present aluminum-surface breakdown/ionization model. The same laser absorption model based on a single ionization formula [7] modified by a tabulated augmentation factor described by Raizer [8] used to simulate multiple ionization effects.

The impulse thrust of the laser Lightcraft Model-200-3/4 was tested using a 10 kW CO_2 pulse laser, which can provide up to 800J for each single pulse, of the Pulsed Laser Vulnerability Test System at the High Energy Laser System Test Facility, White Sands Missle Range, NM. The laser pulse energy was measured with a calorimeter with an estimated uncertainty of ± 10 J in total laser energy delivered. Several variations of the basic Laser Lightcraft design (Model-200 series) similar to those described in Ref. 9 and 10 were tested experimentally. The test results of the 6061-T6 all aluminum Model #200-3/4 vehicle with 18 μs pulse width [10] are chosen for this study. The impulse measurements were conducted with a pendulum apparatus, which has an estimated impulse measurement uncertainty of 1% or better [9,10].

A hybrid unstructured mesh system, shown in figure 1, was generated for the present computation. Also shown, as yellow spots, in figure 1 are the laser traces from the downstream side of the vehicle. Figure 2 shows a close-up view in the cowl region that reveals the hybrid grid arrangement. The element and node numbers for this grid are 26,142 and 14,441 respectively. For spark ignition model, 25% of laser power is assumed as the initial heat source near the focal region. The spark heat source region is bounded by the laser traces and a radius of 1.355 mm from the focal point of the parabolic optical surface of the vehicle. The spark heat source is turned off when the air plasma reaches the self-sustain state (specified as when laser energy absorption efficiency reaches 15%).

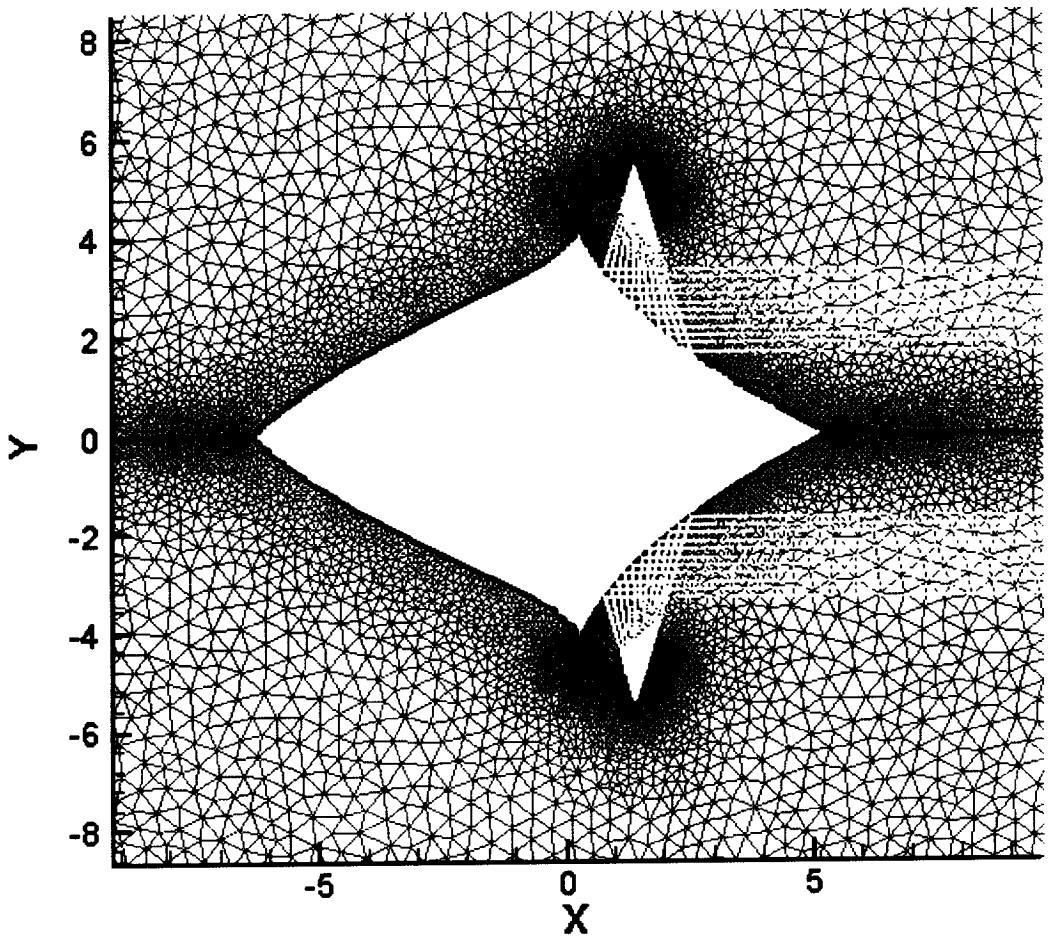

Figure 1. Mesh system and laser traces for the Model-200-3/4 laser Lightcraft.

For the present model, the spark ignition model is totally eliminated. The aluminum surface breakdown/ionization model replaces the air plasma initiation process. Assuming that the aluminum surface emissivity of 0.1, 90 percent of the laser energy is therefore used for the heat-up and breakdown of the aluminum near the focal region. One-dimensional heat conduction equation for the aluminum wall segments, where laser energy absorption is registered, is solved for the time history of the aluminum surface conditions. Surface breakdown and ionization process is then calculated based on the aluminum surface conditions. This provides the electron species production rate in the near wall region, which is responsible for initiating the air plasma. As a result of this model, the surface heat-up time and ionization time scale is directly proportional to the input laser power and the focus condition of laser beam (i.e. better focus produces faster heat-up and plasma iginition).

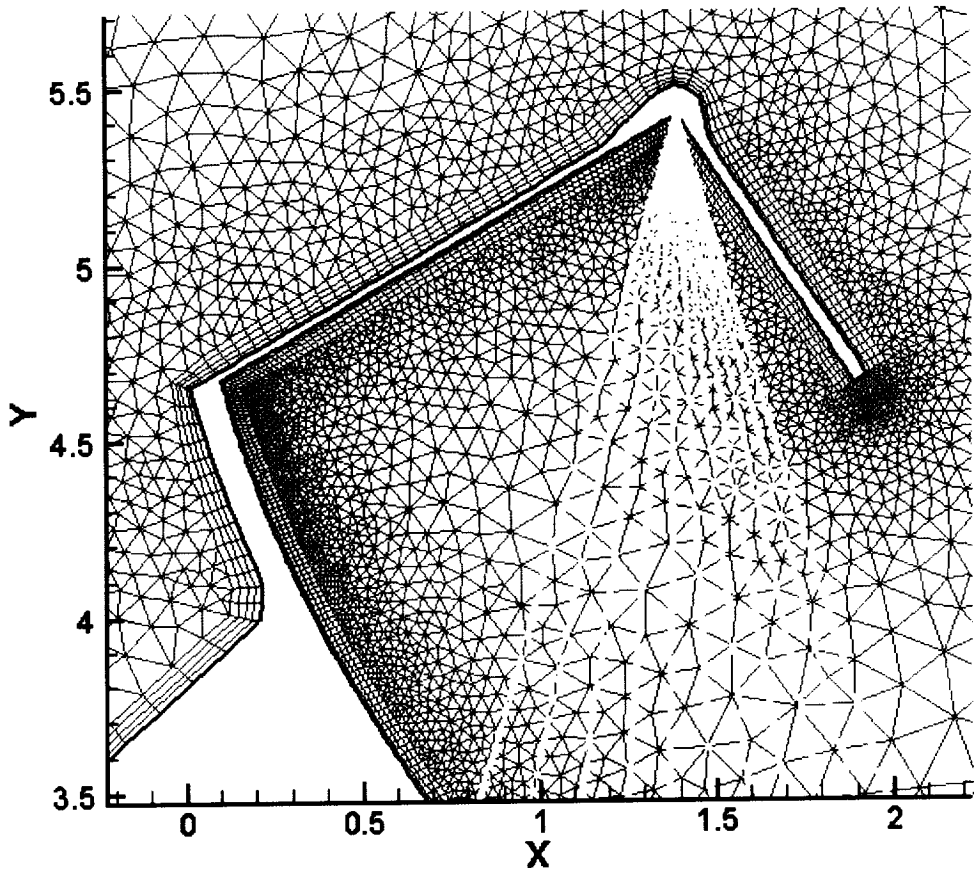

Figure 2. Close-up view of the grid in the cowl region.

In the numerical computations, the initial time step size is specified at 0.05 microseconds and linearly increased to 1 microsecond between 50 to 500 microseconds. This arrangement allow better time resolution for accuracy at the start-up due to expected fast temperature and pressure rise near the focal region and allow better computing time as the blast wave expands and its strength weakened. During every time marching step, the point implicit chemistry solution procedure and the three-temperature coupled equations are solved with reduced time step size based on the chemistry time scale. This multiple time stepping for chemistry is realized to provide the time accuracy for the species equations and has shown great improvement in the smoothness of the flowfield.

During the course of performing the computations, it was found that the pressure and velocity fields near the axis had developed spurious oscillations as the solution proceeded beyond 100 microseconds. The source of this anomaly was traced to be stemming from the cumulative round-off errors in computational cell volume and area calculations. This error becomes obvious for transient flow with quiescent freestream conditions, which is the case for the present application. A better-structured pressure-smoothing scheme is therefore introduced to damp out these background oscillations. Further test of the new scheme has shown good results.

The flowfield solution plots of density, pressure, Mach number, heavy gas temperature, vibrational temperature and electron temperature, for the 400J case at 10 microseconds time level are shown in Figure 3. The laser traces are also shown in the plots. Figure 4 shows the solution plots of pressure, Mach number, heavy gas temperature, vibrational temperature and electron temperature, for the same case as 25 microseconds time level. These plots show the forming and evolution of the blast waves and the high temperature region. The heavy gas temperature is shown to closely follow the distributions of the electron temperature, which is indicative of the very high energy-transfer rate between gas species and electrons for the air plasma. The vibrational temperature follows the blast wave due to shock heating and departure from heavy gas temperature in high temperature region due to increased relaxation time scale.

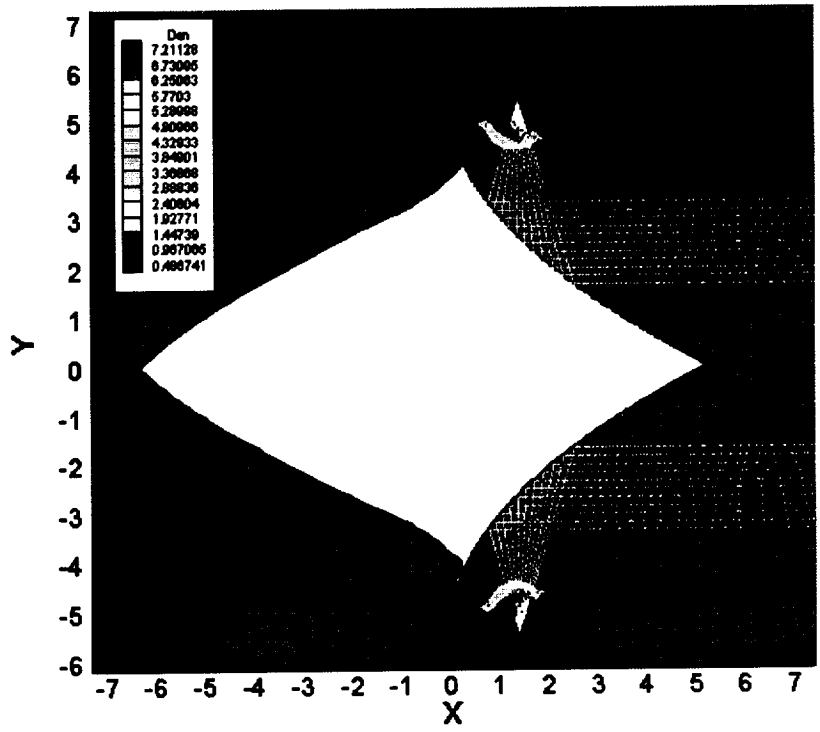

(a) Density, kg/m^3

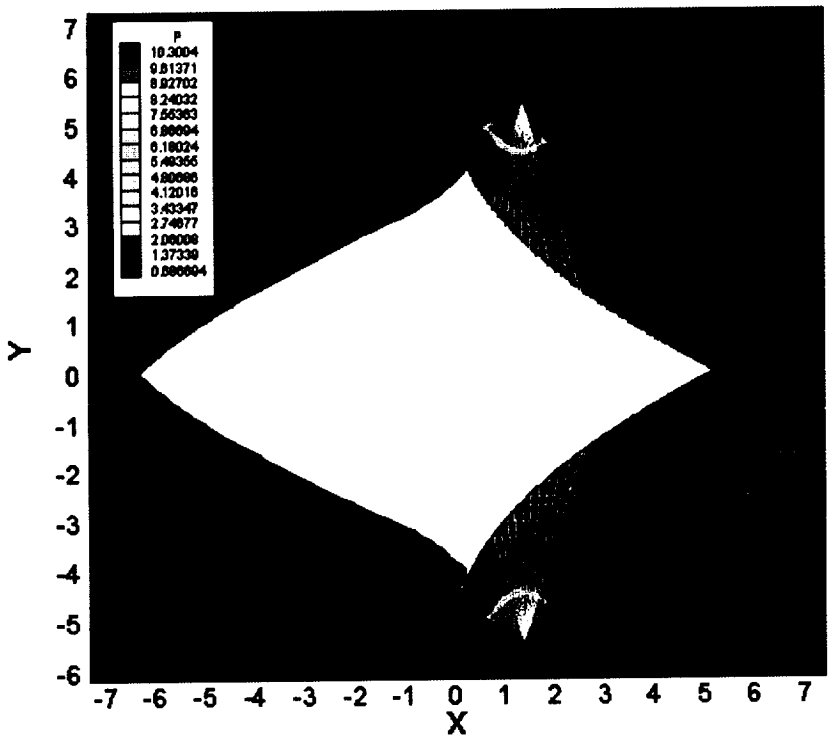

(b) Pressure, ATM

Figure 3. Flowfield solution for 400 J laser energy case at 10 μsec.

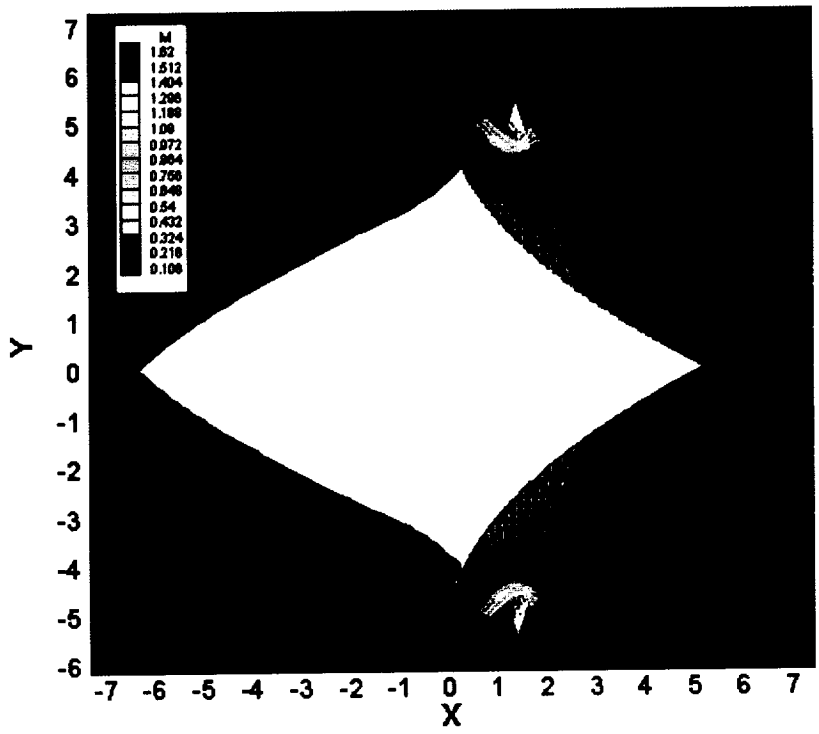

(c) Mach Number

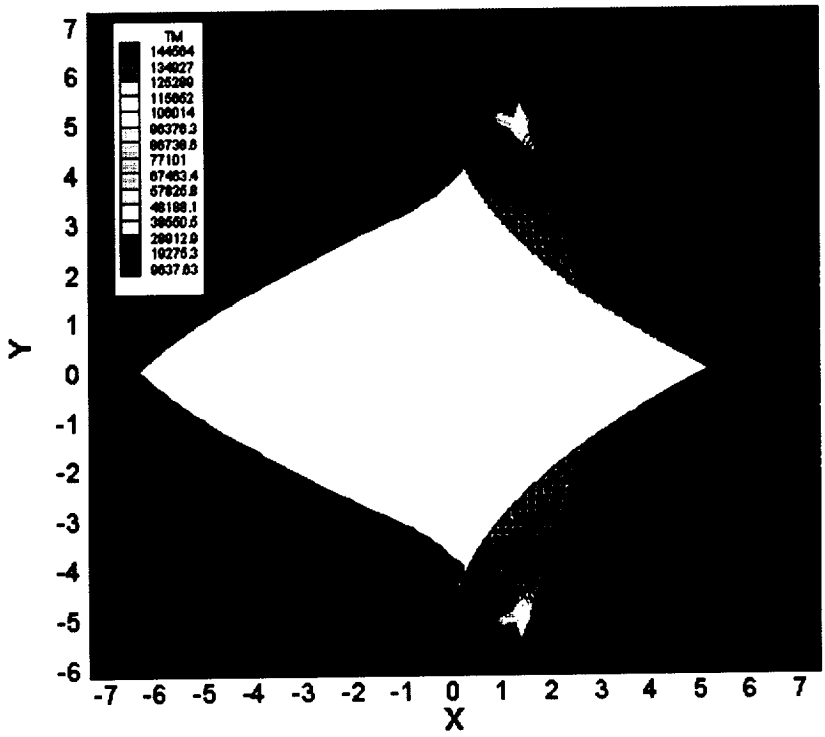

(d) Heavy Gas Temperature, K

Figure 3. (Continued) Flowfield solution for 400 J laser energy case at 10 μsec.

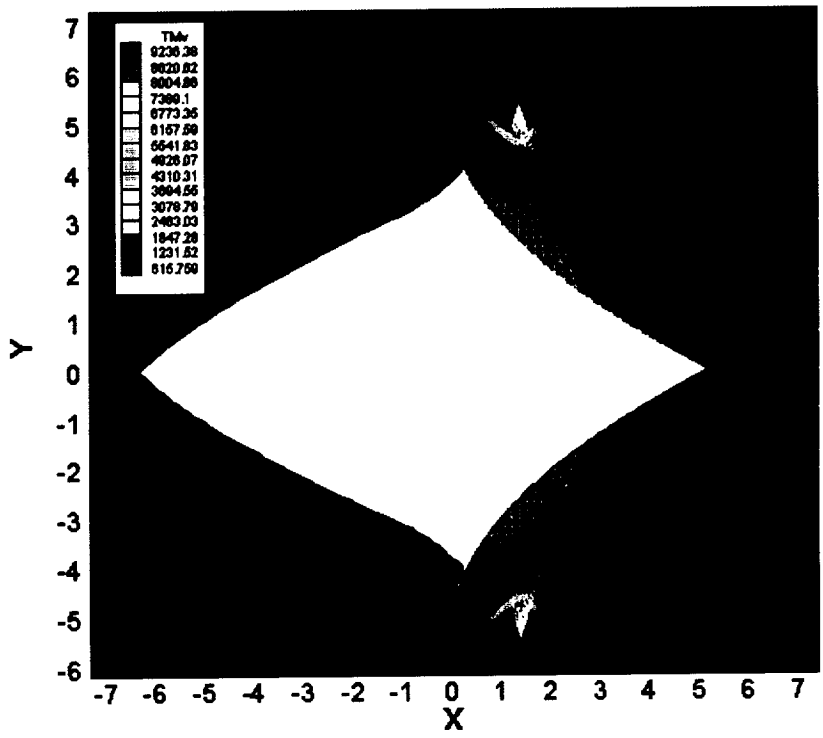

(e) Vibrational Temperature, K

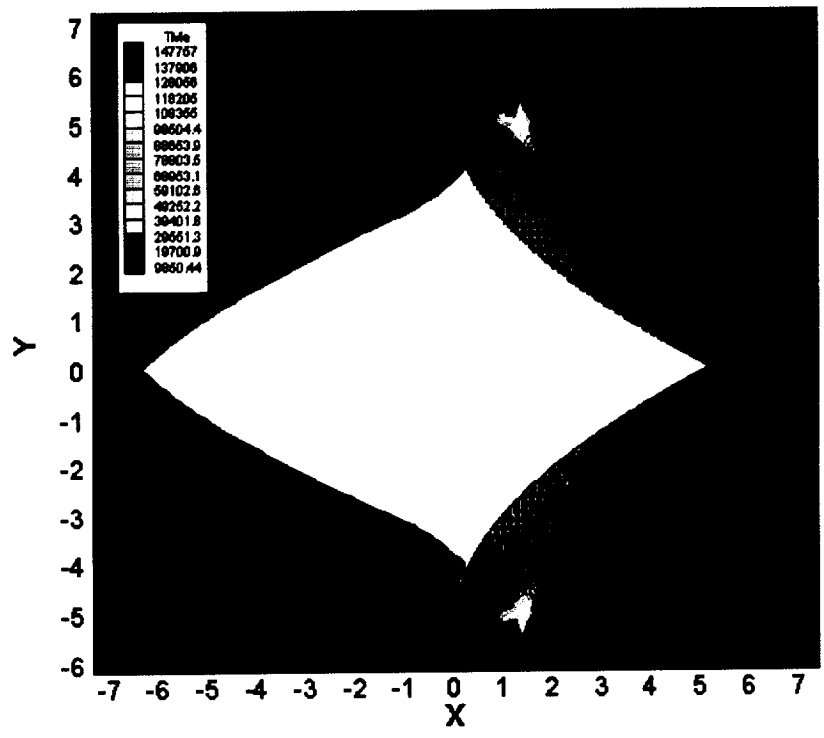

(f) Electron Temperature, K

Figure 3. (Concluded) Flowfield solution for 400 J laser energy case at 10 μsec.

At the beginning, as the shock wave develops, negative thrust is produced due to the shape of cowl inner surface. Later, the shock wave hits the upstream corner of the cavity. As indicated in Figure 4 (a), the pressure level is increased to 41 ATM due to shock reflection off the upstream corner in the cavity. The high-pressure region is attached to the parabolic optical surface. During this time period for the high-pressure wave to travel along the optical surface, the positive thrust is produced and can be referred to as thrust-producing period. As the shock wave expands to wrap around the cowl outer surface and leaves the tip of the optical surface, negative contribution to the thrust will resume until the thrust curve levels off. The evolution of the time-integrated thrust curves for different power levels of the laser is shown in Figure 5 for the present model using aluminum surface breakdown model to initiate the air plasma. The final vehicle thrust coefficients (expressed as coupling coefficient) are then recorded based on the level-off thrust curves and used for data comparisons.

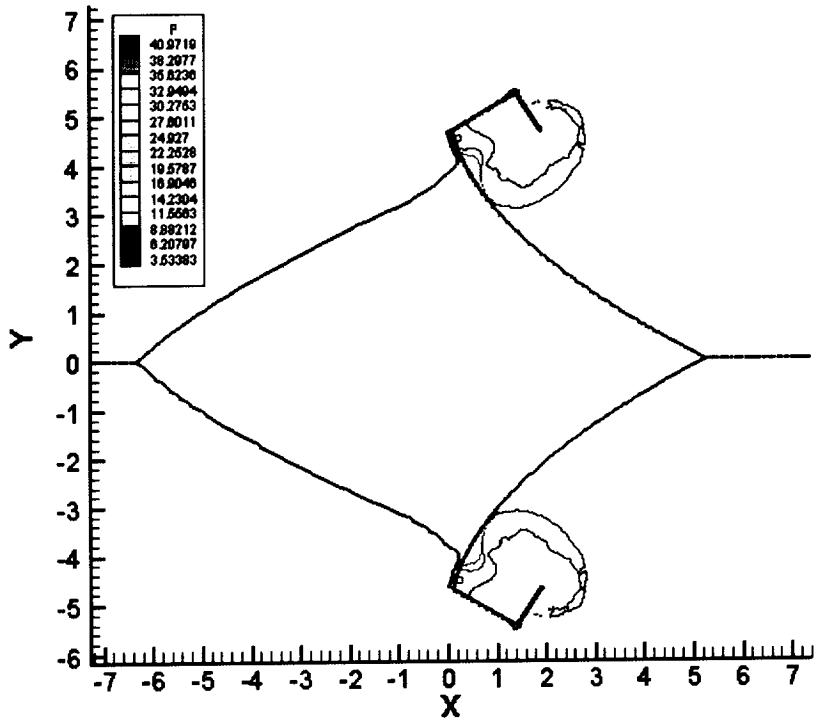

(a) Pressure, ATM

Figure 4. Flowfield solution for 400 J laser energy case at 25 μsec.

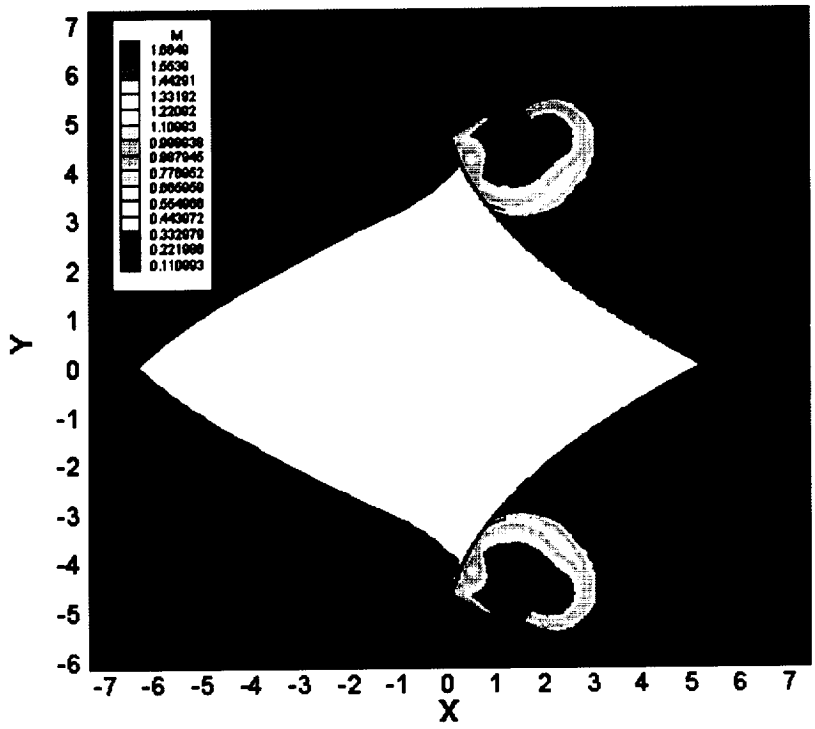

(b) Mach Number

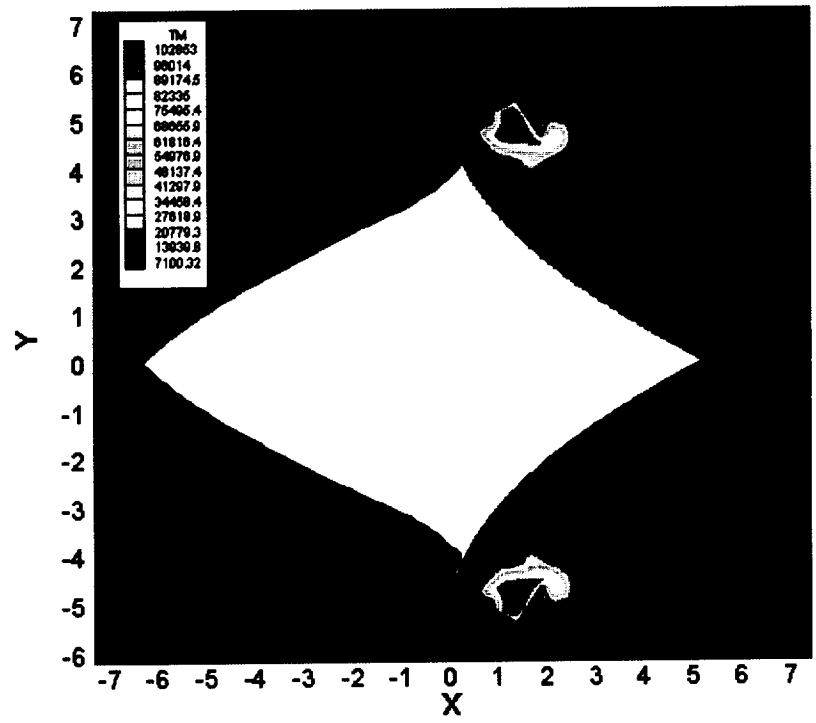

(c) Heavy Gas Temperature, K

Figure 4. (continued) Flowfield solution for 400 J laser energy case at 25 μsec.

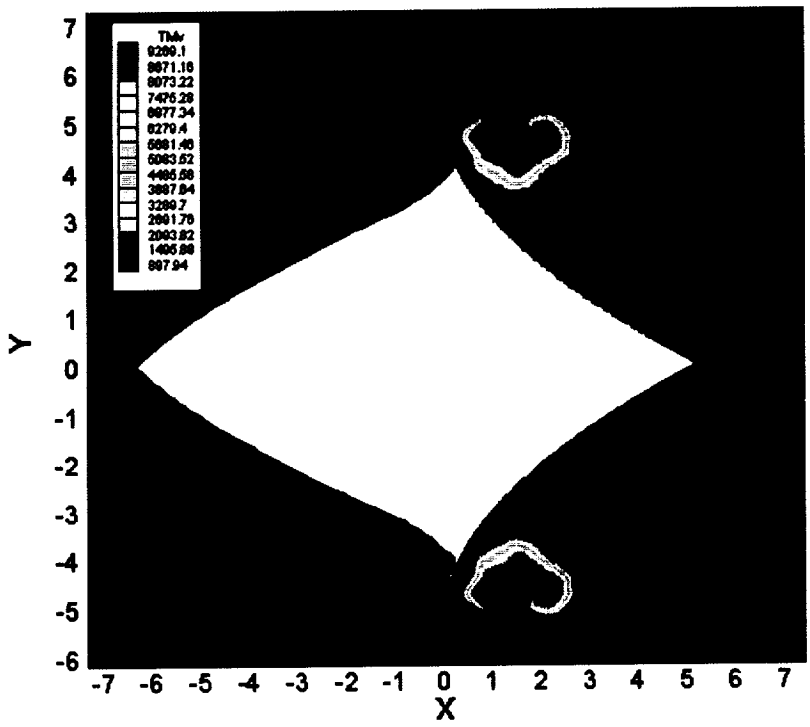

(d) Vibrational Temperature, K

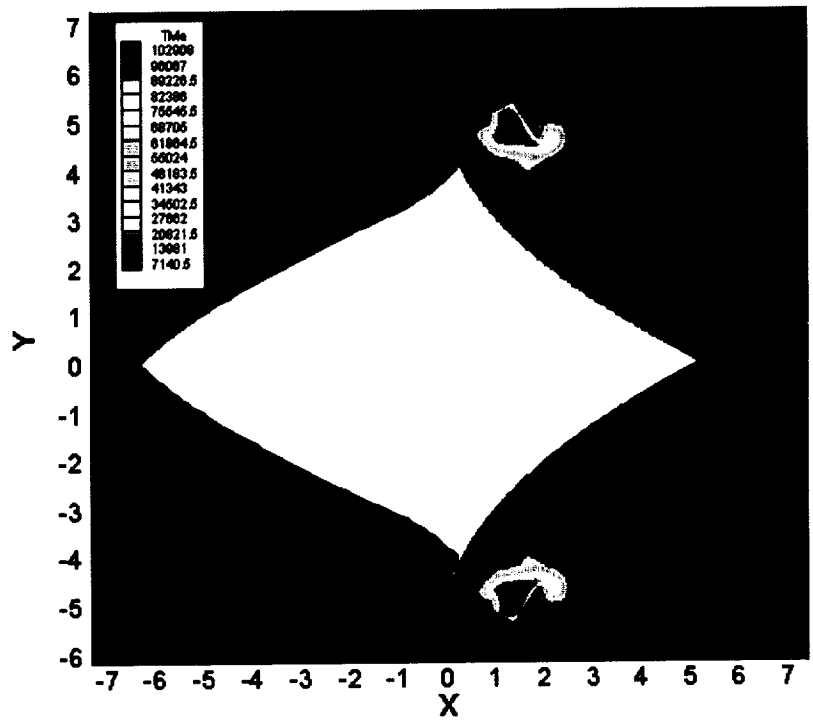

(e) Electron Temperature, K

Figure 4. (Concluded) Flowfield solution for 400 J laser energy case at 25 μsec.

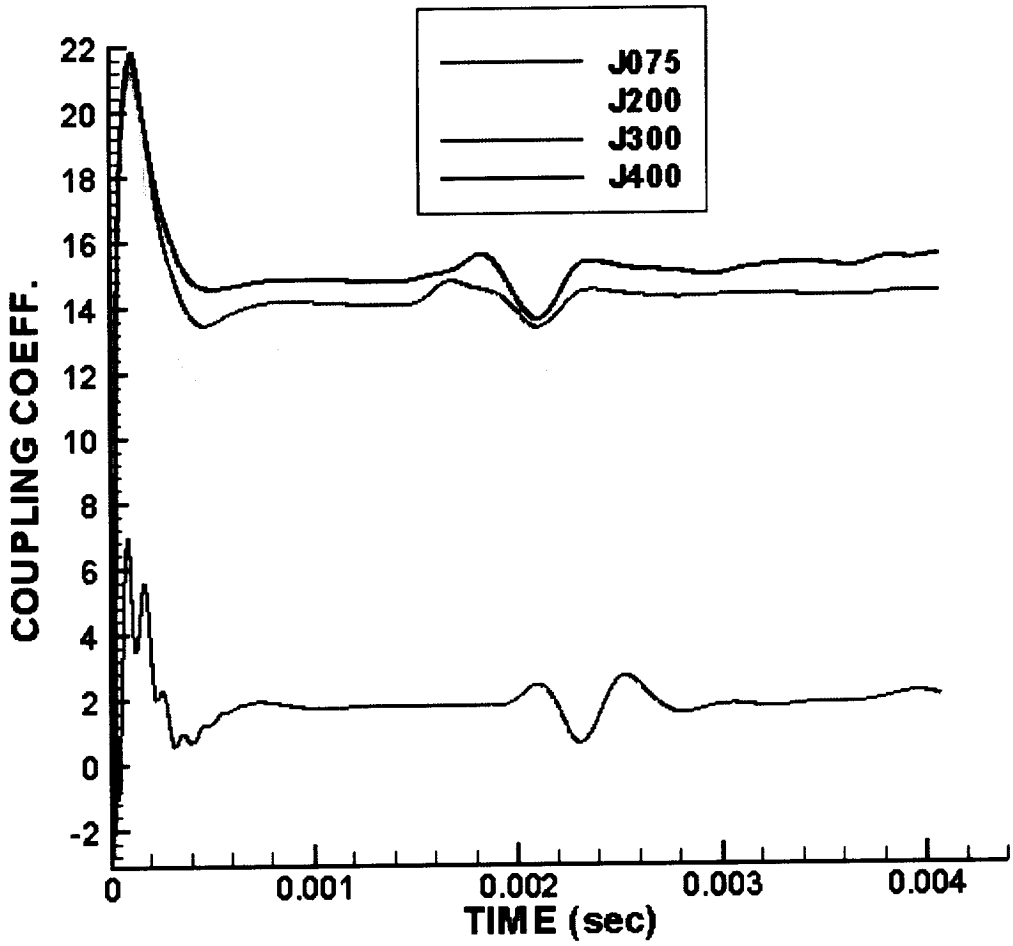

Figure 5. Integrated coupling coefficient time history for different laser input energy of 75J, 200J, 300J and 400J.

The predicted coupling coefficients for the 75J, 200J, 300J and 400J cases are 2.03, 12.7, 14.6 and 15.21 respectively with the present model. These results are consistently lower than the predicted values of the previous model using the spark ignition mechanism. This is understandable since the laser absorption coefficient was tuned for the spark ignition model. Further tuning of the absorption coefficient is needed to fit the present model predictions to the measured data. Figure 6 shows the data comparisons between the predictions of the present and spark ignition models and the experimentally measured data with error bends. The overall trend of the model predictions shows very good correlation with the measured data.

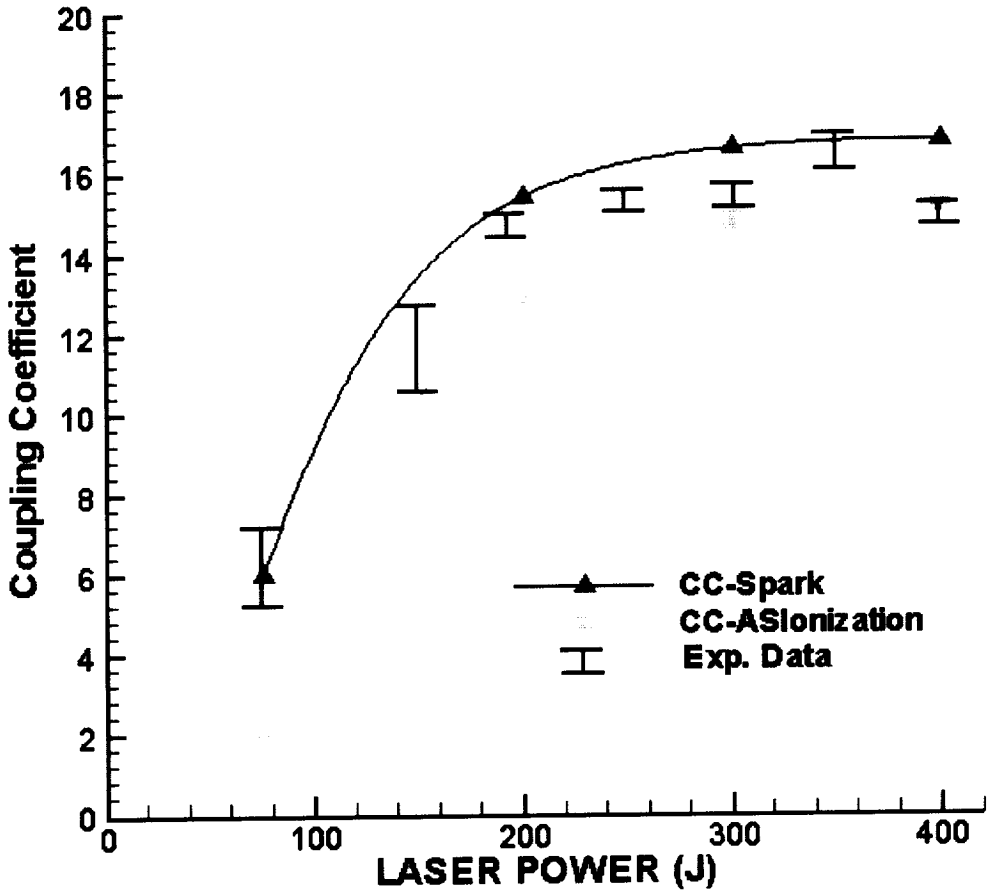

Figure 6. Comparisons of computed and measured coupling coefficients for different laser power levels. CC-Spark stands for the previous model with empirical spark ignition and CC-ASIonization represents the current model with aluminum surface breakdown ionization process.

The impulse thrust of the lightcraft vehicle can be correlated with the laser energy absorption efficiency. This also explains the differences between the predictions of the spark ignition model and the present aluminum-surface breakdown model. Table 3 summaries the energy absorption efficiency of the models and the heat-up time, T, for the present model. Es in Tables is the total energy absorbed by the air plasma. Espark represents the total spark energy required to reach the 15 percent laser absorption efficiency threshold for sustaining the plasma. T (start) indicates when the laser absorption starts and T

(0.001J) signifies the time for the absorbed laser energy reaches 0.001J. It is seen clearly from Table 3 that the heat-up and plasma initiation time is directly proportional to the laser power and the low thrust produced for the present model can be attributed to the lower laser absorption efficiency, Eff, indicated.

Table 3. Energy absorption efficiency and heat-up time scale summary

	Spark Ignition Model			**AL Surface Breakdown/Ionization Model**			
Laser Power	Es (J)	Eff (%)	Espark (J)	Es (J)	Eff (%)	T (start) (sec)	T (0.001J) (sec)
75J	24.12	32.2	2.893	5.27	7.0	4.2×10^{-06}	8.8×10^{-6}
200J	152.04	76.0	4.486	110.40	55.0	1.6×10^{-6}	3.4×10^{-6}
400J	339.92	85,0	5.964	265.02	66.3	0.9×10^{-6}	1.7×10^{-6}

CONCLUSIONS

In the present study, an aluminum surface breakdown/ionization model has been developed and tested for a laser Lightcraft launch vehicle design. The aluminum surface temperature rise due to laser energy input has been modeled using a one-dimensional heat conduction equation with laser radiation heat source applied on the wall surface. An averaged emissivity of 0.1 is assumed for the aluminum surface. The subsequent ionization process near the aluminum surface is calculated based on the wall surface conditions obtained for every time step. This provides the needed electron generation source term near the laser focal region to initiate the air plasma and the associated blast waves. The present model has been demonstrated to replace the need for an artificial spark ignition mechanism as used in the previous model. Hence, this research has provided one step further in making the present analytical model as a true predictive tool for laser supported propulsion system with reduced empiricism.

Benchmark testing of the laser Lightcraft Model-200-3/4 has demonstrated the effectiveness of the present model in predicting the integrated coupling coefficient of the vehicle. The predicted trend is in good agreement with the previous model and the measured data. Further tuning of the modeling constants in estimating the laser absorption coefficient is needed to really fit the present predictions with the measured data. The current development work has laid a concrete foundation for future research in advanced propulsion concepts that may involve short pulses of high intensity energy sources such as microwave, electromagnetism, etc.

REFERENCES

1. Harada, Nob., Kagihiro, M., Shinkai, H., Jiang, W. and Yatsui, K., "Flyer Acceleration by Ablation Plasma Using an Intense Pulsed Ion Beam," AIAA 99-3485, 30th Plasmadynamics and Lasers Conference, 28 June – 1 July, 1999, Norfolk, VA.
2. Harada, Nob., Yazawa, M., Kashine, K., Jiang, W. and Yatsui, K., "Numerical Simulation of Foil Acceleration by Intense Pulsed Ion Beam," AIAA 2000-2272, 31st AIAA Plasmadynamics and Lasers Conference, 19-22 June, 2000, Denver, CO.
3. Harada, Nob., "Acceleration of Multi-Layer Foil by Intense Pulsed Ion Beam," AIAA 2001-3005, 32nd AIAA Plasmadynamics and Lasers Conference, 11-14 June, 2001, Anaheim, CA.
4. Harada, Nob., (Private Communication), September, 2001.
5. Drawin, Hans-Werner and Felenbok, Paul, Data for Plasmas in Local Thermodynamic Equilibrium, Gauthier-Villars, Editeur, Paris, 1965.
6. Reynolds, William C., and Perkins, Henry C., Engineering Thermodynamics, McGraw-Hill Book Company, New York, NY, 1970.
7. Raizer, Y.P., and Tybulewicz, A., "Laser-Induced Discharge Phenomena", *Studies in Soviet Science,* Edited by Vlases, G.C., and Pietrzyk, Z.A., Consultants Bureau, New York, 1977.
8. Zel'dovich, Y.B., and Raizer, Y.P., "Physics of Shock Waves and High Temperature Hydrodynamic Phenomena", Vol. 1, Edited by Hayes, W.D., and Probstein, R.F., Academic Press, New York and London, 1966.
9. Myrabo, L.N., Messitt, D.G., and Mead, F.B., Jr., "Ground and Flight Tests of a Laser Propelled Vehicle," AIAA Paper 98-1001, Jan., 1998.
10. Mead, F.B., Jr., and Myrabo, L.N., Messitt, D.G., "Flight and Ground Tests of a Laser-Boosted Vehicle," AIAA Paper 98-3735, July, 1998.

REPORT DOCUMENTATION PAGE			Form Approved OMB No. 0704-0188

1. AGENCY USE ONLY (Leave Blank)	2. REPORT DATE	3. REPORT TYPE AND DATES COVERED
	June 25, 2002	Final Report

4. TITLE AND SUBTITLE
Laser Induced Aluminum Surface Breakdown Model

5. FUNDING NUMBERS
H-33325D

6. AUTHOR(S)
Yen-Sen Chen, Jiwen Liu and Sijun Zhang

7. PERFORMING ORGANIZATION NAME(S) AND ADDRESS(ES)
Engineering Sciences, Inc.
1900 Golf Road, Suite D, Huntsville, AL 35802

8. PERFORMING ORGANIZATON REPORT NUMBERS

9. SPONSORING/MONITORING AGENCY NAME(S) AND ADDRESS(ES)
George C. Marshall Space Flight Center
Marshall Space Flight Center, AL 35812

10. SPONSORING/MONITORING AGENCY REPORT NUMBER

11. SUPPLEMENTARY NOTES
Ten-See Wang / Technical Monitor

12a. DISTRIBUTION/AVAILABILITY STATEMENT

12b. DISTRIBUTION CODE

13. ABSTRACT ***(Maximum 200 words)***

Laser powered propulsion systems involve complex fluid dynamics, thermodynamics and radiative transfer processes. Based on an unstructured grid, pressure-based computational aerothermodynamics platform, several sub-models describing such underlying physics as laser ray tracing and focusing, thermal non-equilibrium, plasma radiation and air spark ignition have been developed. This proposed work shall extend the numerical platform and existing sub-models to include the aluminum wall surface Inverse Bremsstrahlung (IB) effect from which surface ablation and free-electron generation can be initiated without relying on the air spark ignition sub-model. The following tasks will be performed to accomplish the research objectives.

14. SUBJECT TERMS	15. NUMBER OF PAGES
Laser Propulsion Analysis, Aluminum Surface Breakdown, Ionization Modeling	27
	16. PRICE CODE

17. SECURITY CLASSIFICATION	18. SECURITY CLASSIFICATION OF THIS PAGE	19. SECURITY CLASSIFICATION OF ABSTRACT	20. LIMITATION OF ABSTRACT
Unclassified	Unclassified	Unclassified	Unlimited